Biomaterials 275 (2021) 120962

Contents lists available at ScienceDirect

Biomaterials

journal homepage: www.elsevier.com/locate/biomaterials

NIR-II reinforced intracellular cyclic reaction to enhance chemodynamic therapy with abundant H_2O_2 supply

Yuling He [a], Shuwen Guo [c], Yue Zhang [a], Ying Liu [a,b,*], Huangxian Ju [a]

[a] State Key Laboratory of Analytical Chemistry for Life Science, School of Chemistry and Chemical Engineering, Nanjing University, Nanjing, 210023, China
[b] Chemistry and Biomedicine Innovation Center, Nanjing University, Nanjing, 210023, China
[c] State Key Laboratory of Quality Research in Chinese Medic, Institute of Chinese Medical Sciences, Macau University, Macao, 999078, China

ARTICLE INFO

Keywords:
Chemodynamic therapy
H_2O_2 supplement
NIR-II light Irradiation
Metal-organic coordinated nanoparticle
Photothermal effect

ABSTRACT

Chemodynamic therapy (CDT) is an ideal therapeutic modality with endogenous H_2O_2 as stimulus. Most intracellular H_2O_2 supplement strategies for improving CDT efficiency are strongly rely on oxygen participation, and the hypoxia tumor microenvironment impairs their performance. Here we develop a self-assembled metal-organic coordinated nanoparticle Cu–OCNP/Lap with NIR-II reinforced intracellular cyclic reaction to enhance CDT efficiency. Cu–OCNP/Lap is synthesized using Cu^{2+} as nodes and 1,4,5,8-tetrahydroxyanthraquinone (THQ) and banoxantrone dihydrochloride (AQ4N) as ligands, with β-lapachone (β-Lap) loading to conduct intracellular cyclic reaction. Cu–OCNP/Lap has good photothermal effect at NIR-II window, and the corresponding local temperature increase speeds blood flow and supplies sufficient oxygen at tumor site to reinforce β-Lap cyclic reaction with abundant H_2O_2 generation. Cu^{+} is released from Cu–OCNP/Lap in response to glutathione (GSH) and triggers CDT. Sufficient intracellular H_2O_2 supply enhances CDT effect and demonstrates good suppressions for tumor growth. This design offers a promising strategy to enhance CDT efficiency.

1. Introduction

Chemodynamic therapy (CDT) converts tumor endogenous H_2O_2 to highly cytotoxic hydroxyl radical (•OH) via the transition-metal-mediated Fenton reaction or Fenton-like reaction [1–3], and induces cell apoptosis [4,5]. With high tumor specificity and less limitation on therapeutic depth, it has emerged as a promising anticancer modality [6,7].

Although tumor microenvironment (TME) is featured in higher H_2O_2 level compared with normal cells, it is still insufficient to generate vast •OH to achieve satisfactory therapeutic efficiency of CDT [8–11]. Endowing CDT agents with H_2O_2 supplementing capability is often used to enhance their anticancer efficiency [12–14]. Oxidase catalytic reactions with endogenous substrates have been used to elevate intracellular H_2O_2 concentration [15–17], including glucose oxidase (GOD) [12,18], choline oxidase (COx) [19], and the cascade catalytic reactions of NADPH oxidase (NOX) and superoxide dismutase (SOD) [20]. However, most oxidase catalytic reactions require oxygen intensive participation or directly acting as reaction substrate. The intracellular hypoxia environment and continuous consumption of reaction substrate without regeneration limited intracellular H_2O_2 supply, thus impaired CDT enhancement effect [21,22]. Thus, there is a great need for new CDT agents with efficient H_2O_2 generation capability in hypoxia environment.

Tumor cell overexpressed nicotinamide adenine dinucleotide (phosphate) (NAD(P)H):quinone oxidoreductase-1 (NQO1) enzyme could convert β-lapachone (β-Lap) to hydroquinone [23,24]. The intracellular β-Lap cyclic reaction is completed by oxygen participation to oxidize hydroquinone back to β-Lap with H_2O_2 generation. Though enzyme substrate is regenerated in the cyclic reaction, hypoxia microenvironment still impedes reaction efficiency. Taking advantages of the higher penetration depth and less tissue absorption and scattering of NIR-II light, here we developed a NIR-II reinforced intracellular β-Lap cyclic.

reaction with abundant H_2O_2 supply to enhance CDT efficiency. A self-assembled metal-organic coordinated nanoparticle was synthesized with Cu^{2+} as nodes and molecules 1,4,5,8-tetrahydroxyanthraquinone (THQ) and banoxantrone dihydrochloride (AQ4N) as organic ligands (Cu-THQ/AQ4N). Cu-THQ/AQ4N was loaded with β-Lap and wrapped with folic acid functionalized polyethylene glycol (PEG-FA) for

* Corresponding author. State Key Laboratory of Analytical Chemistry for Life Science, School of Chemistry and Chemical Engineering, Nanjing University, Nanjing, 210023, China.
E-mail address: yingliu@nju.edu.cn (Y. Liu).

https://doi.org/10.1016/j.biomaterials.2021.120962
Received 11 January 2021; Received in revised form 26 May 2021; Accepted 4 June 2021
Available online 11 June 2021

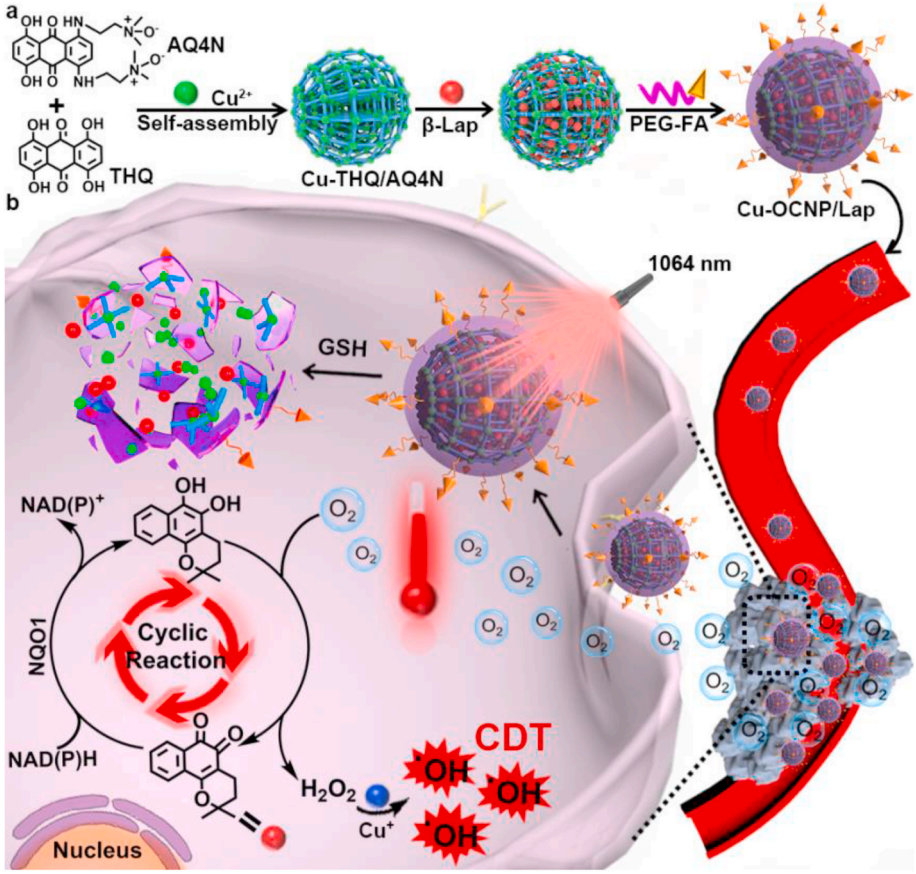

Scheme 1. Schematic illustration of (a) synthesis of Cu–OCNP/Lap and (b) its intracellular delivery and NIR-II reinforced intracellular β-Lap cyclic reaction with abundant H_2O_2 supply to enhance CDT.

extending circulation time and enhancing tumor targeting (Scheme 1a). After the as-obtained Cu–OCNP/Lap entered tumor cells, they were exposed under 1064 nm light irradiation. Cu–OCNP/Lap had impressive photothermal conversion efficiency and resulted good photothermal effect at NIR-II window, which increased local temperature of tumor and accelerated blood flow, thus effectively improved tumor oxygen content [25]. Tumor cell overexpressed glutathione (GSH) reduced Cu^{2+} to Cu^{+} [26], and resulted the degradation of Cu–OCNP/Lap with release of Cu^{+} and β-Lap to trigger intracellular cyclic reaction. The enhanced intracellular oxygen supply effectively reinforced β-Lap cyclic reaction and resulted abundant intracellular H_2O_2 accumulation, which facilitated Cu^{+} Fenton-like reaction and effectively enhanced CDT efficiency (Scheme 1b). In addition, the consumption of GSH during Cu–OCNP/Lap decompose process relieved antioxidant defense of TME and further enhanced therapeutic efficiency [27,28]. The efficient intracellular H_2O_2 supply strategy via NIR-II reinforced cyclic reaction provided an effective approach to enhance CDT, and would potentially benefit clinical application.

2. Experimental section

2.1. Materials

Methylene blue (MB) and 1,4,5,8-tetrahydroxyanthraquinone (THQ) were purchased from J&K Chemical Co (Beijing, China). Banoxantrone dihydrochloride (AQ4N) and β-lapachone (β-Lap) were purchased from Sigma-Aldrich (USA). Amino terminated polyethylene glycol PEG-NH_2 (Mw 2000) and polyethylene glycol modified with folate (PEG2000-FA) or fluorescein isothiocyanate (PEG-FITC) (Mw 2000) were purchased from ToYong Biotech (Shanghai, China). 2′,7′-dichlorofluorescein diacetate (DCFH-DA) was obtained from Invitrogen Life Technologies (USA). Dulbecco's modified eagle's medium (DMEM), 4,6-diamidino-2-phenylindole (DAPI), Calcein-AM/PI double stain kit, trypsin, 3-[4,5-dimethylthiazol-2-yl]-2,5-diphenyltetra-zoliumbromide (MTT), penicillin streptomycin, fetal bovine serum (FBS), phosphate buffered saline (PBS, pH 7.2) were purchased from KeyGEN BioTECH (Nanjing, China). Reduced glutathione (GSH) assay kit was purchased from Beijing Solarbio Science & Technology Co. ROSGreen H_2O_2 probe was came from purchased from Maokang Co., Ltd. (Shanghai,China). Copper chloride dehydrate, N-Ethylmaleimide (NEM) and trimethylamine were purchased from Alfa Aesar (Shanghai, China). All other reagents and solvents were of analytical grade and used directly.

2.2. Apparatus

Transmission electron microscopic (TEM) images were acquired by JEM-2100 transmission electron microscope (JEOL Ltd., Japan). Dynamic light scattering (DLS) analysis was performed with Zeta Plus 90 Plus/BI-MAS (Brook haven, USA). UV–Vis absorption spectra were recorded with Nanodrop-2000C UV–Vis spectrophotometer (Nanodrop, USA). Fourier-transform infrared (FT-IR) spectra were recorded with Nicolet 6700 spectrophotometer (Nicolet, Canada). X-ray photoelectron spectroscopy (XPS) was performed by Thermo ESCALAB 250XI (Thermo-Fisher, United States). Fluorescence spectra were recorded with F-7000 spectrofluorophotometer (HITACHI, Japan). Confocal fluorescence images were acquired on TCS SP5 confocal laser scanning microscope (Leica, Germany). MTT assay was performed on Hitachi/Roche System Cobas 6000 (Bio-Rad, USA). Zeta potential was acquired by using Malvern Zetasizer Nano ZS90 at RT. Concentration of copper was measured by the inductively coupled plasma-mass spectrometer

(ICP-MS, Avio500, USA). Nitrogen (N_2) adsorption desorption isotherm curves and the corresponding pore-size distributions were obtained using a TriStar 3000 (Micromeritics, Norcross, GA, USA) surface area analyzer.

2.3. Synthesis of Cu-organic coordinated nanoparticle (Cu–OCNP)

1.5 μL THQ (50 mg/mL) was mixed with 1 mL ethanol, 10 μL AQ4N (10 mg/mL) and 60 μL $CuCl_2$ (4 mg/mL) were subsequently added, and the pH of mixture solution was adjusted to 7.2 using trimethylamine. After stirring for 2 h, the reaction solution was centrifuged for 5 min at 14000 rpm, and the obtained Cu-THQ/AQ4N organic coordinated nanoparticle was washed thrice with ethanol, and redispersed in 1 mL ethanol. PEG-NH_2 was modified to Cu-THQ/AQ4N via coordination interaction between Cu^{2+} and $–NH_2$. 4 mL PEG-NH_2 (5 mg/mL) was added into the above obtained solution, stirred overnight at room temperature, and centrifuged for 5 min at 13000 rpm. The as-obtained Cu–OCNP was washed thrice with DI-water and dispersed in PBS buffer (pH 7.4) for further usage.

2.4. Preparation of β-lap loaded Cu–OCNP (Cu–OCNP/Lap)

β-Lap (2 mg/mL, 200 μL) in ethanol was mixed with Cu-THQ/AQ4N dispersed in ethanol. After stirring for 8 h, 4 mL PEG-NH_2 (5 mg/mL) was added into the above reaction solution, and stirred for 12 h at room temperature. 10 mL water was then added to the reaction mixture, and continuously stirred for 12 h at the room temperature. The obtained product was centrifuged for 5 min at 13000 rpm, and washed with ethanol and DI-water thrice. The as-obtained Cu–OCNP/Lap was dispersed in PBS buffer (7.4) and characterized by UV–Vis spectrum.

2.5. The evaluation of photothermal effect

To evaluate the photothermal (PTT) performance in vitro, 1 mL Cu–OCNP aqueous solution with various concentrations (50, 100, 150, 200 μg/mL) were irradiated with 1 W/cm^2 1064 nm laser for 6 min, and the real-time temperature of aqueous solution was recorded by an infrared thermal imaging camera at an interval of 10 s. The photothermal stability was further studied via continuously measuring solution temperature until cooling period for 10 min after removing laser irradiation. The same processes were repeated four times.

To measure the photothermal conversion efficiency, 50 μg/mL Cu–OCNP was exposed to 1064 nm laser at the power of 1 W/cm^2 for 6 min, and then the laser was removed for cooling down the temperature of solution to room temperature, and the real-time temperature of solution was measured by infrared thermal imaging camera.

The photothermal conversion efficiency (η) was calculated according to equation (1) with a previously reported method [29,30]:

$$\eta = \frac{\mathrm{hs}(T_{Max} - T_{Surr}) - Q_{Dis}}{\mathrm{I}\left(1 - 10^{-A_{1064}}\right)} \quad (1)$$

where h is the heat transfer coefficient, s is the surface area of the container, and the value of hs is determined from equation (2). Q_{Dis} is the heat associated with solvent absorbance, which is measured as 25.2 mW with deionized water as solvent. I is the laser power (1 W/cm^2) and A_{1064} is the absorbance of Cu–OCNP at 1064 nm.

$$hs = \frac{\mathrm{mC}}{\tau s} \quad (2)$$

m is the mass of solution, C is the specific heat capacity of water (4.2 J g^{-1}), and τs is time associated constant, which is determined from equation (3) by applying the time data versus $-\ln\theta$ from the cooling period.

$$t = -\tau s\, In(\theta) \quad (3)$$

θ is a dimensionless parameter, known as the driving force temperature, and is calculated using equation (4).

$$\theta = \frac{\mathrm{T} - T_{Surr}}{T_{Max} - T_{Surr}} \quad (4)$$

T_{Max} and T_{Surr} are the maximum steady state temperature and the environmental temperature, respectively.

2.6. Characterization of Cu–OCNP degradation

To study the effect of pH on Cu–OCNP degradation, 0.1 mg Cu–OCNP was dispersed in 1 mL PBS of different pH (7.4, 6.5 5.0), and incubated at 37 °C for different times. To study the effect of GSH on Cu–OCNP degradation, 0.1 mg Cu–OCNP was dispersed in 1 mL PBS (pH 6.5) containing GSH (10 mM), and incubated at 37 °C for different times. The fluorescence recovery of AQ4N was measured at 640–700 nm, and the AQ4N release percentage was calculated via comparing fluorescence of released AQ4N with fluorescence of total AQ4N.

Copper ion release was also quantified to characterize Cu–OCNP degradation. 0.4 mg Cu–OCNP was dispersed in 2 mL PBS at pH 6.5 containing 10 mM GSH, and incubated at 37 °C. At predetermined time intervals, Cu–OCNP solution was centrifuged at 14000 rpm for 6 min, and the supernatant containing released copper ion was collected for ICP-MS spectrum measurement. The released copper ion percentage was calculated by comparing the amount of released copper ion with the total amount of copper ion. The same experiment was also performed in the absence of GSH for negative control.

2.7. Measurement of •OH generation

1 mL of Cu–OCNP (0.1 mg/mL, pH 6.5) was incubated with GSH (4.0 mM) at 37 °C for 12 h, 500 μM of H_2O_2 and 4 μL of MB (10 μg/mL) were added and continuously incubated at 37 °C for 30 min. The absorbance change of MB was detected at 665 nm by UV–Vis spectrum to characterize •OH generation. To test the contribution of PTT effect to •OH generation, the same experiment was performed with 6 min 1064 nm laser (1 W/cm^2) irradiation.

Electron paramagnetic resonance (EPR) spectroscopy was also employed to verify •OH generation with 5,5-Dimethyl-1-pyrroline N-oxide (DMPO) as a spin trapping agent for •OH. 100 μL Cu–OCNP (0.1 mg/mL, pH 6.5) was mixed with 4 mM GSH, and incubated at 37 °C for 2 h 500 μM H_2O_2 was then added, and irradiated with 1064 nm light for 6 min. After adding 50 μL DMPO (100 mM) to the above mixture solution, it was transferred into a quartz capillary using capillarity for EPR spectrum measurement, which was performed at room temperature in perpendicular mode on a Bruker EMX-8/2.7 spectrometer and recorded with the following settings: microwave frequency = 9.872 GHz, microwave power = 6.375 mW, modulation frequency = 100.00 kHz and modulation amplitude = 1.00 G. The control experiment was performed with the same reaction procedure in the absence of 1064 nm light irradiation.

2.8. Cell culture

HeLa cell line (cancer cell) and NIH 3T3 cell line (normal cell) were incubated with DMEM medium containing 10% FBS and 1% penicillin-streptomycin (10000 U/mL) at 37 °C in a humidified atmosphere containing 5% CO_2.

2.9. Intracellular fluorescence recovery of AQ4N

AQ4N fluorescence was recovered upon Cu–OCNP degradation in response to intracellular GSH. HeLa cells were treated with Cu–OCNP (20 μg/mL) for different times (4 and 8 h) at 37 °C, washed twice with PBS, and visualized by 633 nm excitation for AQ4N. Control experiment was performed by pretreated HeLa cells with GSH scavenger N-

ethylmaleimide (NEM, 30 μM) for 1 h at 37 °C to suppress intracellular GSH expression, and continuously incubated with Cu–OCNP (20 μg/mL) for 8 h before AQ4N fluorescence recovery measurement.

2.10. Intracellular GSH quantification

HeLa cells were seeded in 6-well plate at a density of 1×10^6 cells/well, and cultured in 5% CO_2 at 37 °C for 24 h. The cell culture medium was then replaced with fresh DMEM containing Cu–OCNP/Lap (20 μg/mL), continuously cultured for 4 h, and irradiated with 1064 nm light for 15 min. After continuously culturing for 8 h, the corresponding cells were collected and centrifuged at 1500 rpm for 15 min at 4 °C. After removing the supernatant, the as-obtained cells were dispersed in PBS, froze by liquid nitrogen, and thawed at 37 °C. The as-obtained samples were centrifuged at 10000 rpm for 10 min at 4 °C, and GSH and GSSH in supernatant was quantified with GSH assay kit according to the manufacturer's protocol.

2.11. Intracellular •OH imaging

HeLa cells were incubated with Cu–OCNP and Cu–OCNP/Lap in 1% O_2 condition (20 μg/mL) for 6 h, the culture medium was then replaced with fresh DMEM containing ROS probe 2′,7′-dichlorofluorescein diacetate (DCFH-DA) to image intracellular •OH generation. After continuously cultured for 30 min, the cells were washed with PBS, and followed by taking green fluorescence at 488 nm excitation using CLSM. HeLa cells were incubated with Cu–OCNP/Lap (20 μg/mL) in 21% O_2 condition with or without 1064 nm light for 10 min, and subsequently treated with DCFH-DA to demonstrate PTT effect on •OH generation.

2.12. Cell viability assay

The cytotoxicity of Cu–OCNP/Lap was evaluated via MTT assay. NIH 3T3 cells at a density of 1×10^4 cells/well were seeded in 96-well plates and incubated for 24 h. The cell culture medium was then replaced with fresh DMEM containing serial concentrations of Cu–OCNP/Lap (10, 20, 30, 40, 50 μg/mL), and continuously incubated for 24 h. Subsequently, 20 μL MTT (5 mg/mL) was added into each well, and incubated for 4 h. After removing culture medium, 80 μL DMSO was added to dissolve the crystal precipitates, and the optical density was measured at 490 nm with a Bio-Rad microplate reader. The relative cell viability was calculated by ($A_{test}/A_{control}$) x 100%. NIH 3T3 cells incubated with PBS in the absence of Cu–OCNP/Lap were served as controls.

HeLa cells were also treated with free β-Lap, Cu–OCNP/Lap, Cu–OCNP/Lap with 1064 nm light irradiation in normoxia environment, and the cell viability were evaluated using MTT assay with the above procedure. PBS treated HeLa cells in the presence of 1064 nm laser irradiation were served as controls, and Cu–OCNP, Cu–OCNP/Lap treated cells in hypoxia environment was also evaluated. To confirm the therapeutic efficiency of PTT alone, HeLa cells were pretreated with 50 μM GSH scavenging reagent N-ethylmaleimide (NEM) for 1 h, and then incubated with Cu–OCNP/Lap in the presence of 1064 nm light. The cell viability was measured with the same procedure above.

Live/dead dual staining assays were further preformed to verify the therapeutic efficiency of Cu–OCNP/Lap. HeLa cells were incubated with Cu–OCNP and Cu–OCNP/Lap in hypoxia or normoxia environment. The culture medium was discarded, and the cells were washed thrice with PBS, and stained with calcein-AM (10 nM) and PI (4 μM) solution for 20 min at 37 °C. CLSM images were then taken after washed the cells with PBS. Moreover, Cu–OCNP/Lap in the presence of 1064 nm light incubated HeLa cell group and NEM pretreated HeLa cell group were also performed.

2.13. Animal tumor xenograft models

All animal experiments were approved by the Model Animal Research Center of KeyGEN BioTECH and followed the Institutional Animal Use and Care Regulations. Specific pathogen-free female BALB/c nude mice (6–8 weeks old, ~20 g) were fed with normal conditions. The tumor models were established by subcutaneous injection of HeLa cells (1.0×10^7 cells/mL) into the selected positions of nude mice. In vivo therapy was applied when tumor volume reached 80 mm^3.

2.14. In vivo fluorescence and PA imaging of tumor-bearing mice and imaging of temperature change

The HeLa tumor-bearing mice were intravenously administrated with Cu–OCNP/Lap (5 mg/kg). Fluorescence and PA imaging of mice were respectively acquired using IVS animal imaging system and photoacoustic (PA) imaging system at different time points post injection (0, 3, 6, 10 16 and 24 h). In addition, the mice were irradiated with 1064 nm laser for 6 min at tumor grown positions at 10 h post injection, and the tumor temperature of mice was measured with infrared thermal imaging camera. The tumor temperature of mice with PBS treatment was served as control group.

2.15. In vivo imaging of hemoglobin oxygen saturation

Hemoglobin oxygen saturation (sO_2) in the tumor area was monitored using photoacoustic (PA) imaging system. The HeLa tumor-bearing mice were intravenously administrated with Cu–OCNP/Lap (5 mg/kg). The mice were irradiated with 1064 nm laser for 10 min at tumor grown positions at 10 h post injection, and sO_2 of tumor site were collected by PA imaging system. sO_2 of tumor site before Cu–OCNP/Lap injection was recorded as the background signal.

2.16. In vivo hypoxia and H_2O_2 accumulation evaluation

Immunofluorescence staining was utilized to evaluate *in vivo* hypoxia condition and H_2O_2 accumulation. The HeLa tumor-bearing mice were intravenously administrated with Cu–OCNP/Lap (5 mg/kg), and irradiated with 1064 nm laser for 15 min at tumor grown position at 10 h post injection. The mice were continuously fed and sacrificed at 24 h. The collected tumors were fixed with 4% paraformaldehyde, embedded in paraffin, sliced, stained with HIF-1α according to the procedure provided by the manufacturers. CLSM image were taken for the staining tumor slices. Moreover, the frozen section of tumors was stained with ROSGreen H_2O_2 probe, and taken by CLSM image.

2.17. In vivo antitumor therapy

The tumor-bearing mice were divided into five groups randomly, and intravenously administrated with PBS, Cu–OCNP, Cu–OCNP (NIRII irradiation), Cu–OCNP/Lap, Cu–OCNP/Lap (NIR II irradiation) for each mice group, respectively. The irradiation groups were exposed to 1064 nm laser at power of 1.0 W/cm^2 for 15 min at tumor grown positions 10 h post injection. The injection and irradiation were repeated every other two days for five times. The tumors were measured by a Vernier caliper, and the volumes were calculated as $V = (L \times W^2)/2$, in which L and W are the length and width of the tumor, respectively. In addition, the mouse body weights for each group were recorded during 16 days. All mice were sacrificed after treatment for 16 days, and the collected tumors were fixed with paraformaldehyde, embedded in paraffin, sliced, stained with Hematoxylin-Eosin (H&E) and TUNEL, and observed via fluorescence microscopy (IX71, Olympus). The histopathological analysis of normal organs (liver, lung, spleen, heart, and kidney) was also performed at 16 days according to the same procedure mentioned above.

2.18. Hemolysis assay of Cu–OCNP/Lap

Blood samples from healthy mouse were collected in a container

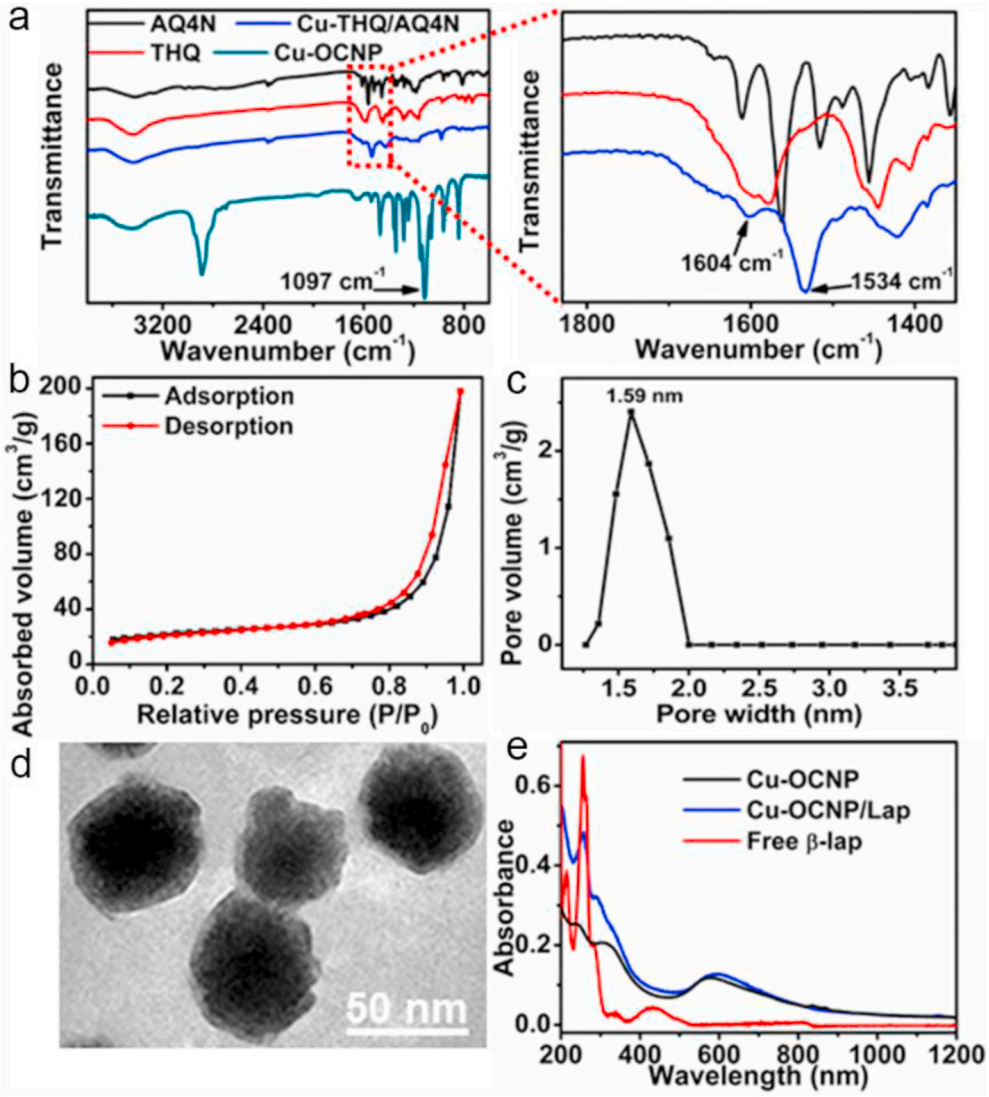

Fig. 1. a) FT-IR spectra of AQ4N, THQ, Cu-THQ/AQ4N, Cu–OCNP, b) N_2 adsorption-desorption isotherms and (c) pore size distribution of Cu-THQ/AQ4N, d) TEM image of Cu–OCNP/Lap, e) UV–Vis spectra of Cu–OCNP, Cu–OCNP/Lap, and free β-Lap.

filled with heparin, and centrifuged at 1500 rpm for 10 min to obtain red blood cells (RBCs). After washed and diluted with PBS, RBCs (200 μL) was mixed with 800 μL Cu–OCNP/Lap dispersed PBS with different concentrations (200, 400, 600, 800, 1000 μg/mL), and incubated at 37 °C. After incubation for 3 h, the mixture solutions were centrifuged, and the supernatants absorptions were measured at 570 nm (A_{sample}). Meanwhile, RBCs were mixed with PBS and water as negative control (A_{PBS}) and positive control (A_{water}), respectively. The hemolysis percentages were calculated by (A_{sample}-A_{PBS})/(A_{water}-A_{PBS}) x 100%.

2.19. Biochemistry analysis of Cu–OCNP/Lap

Healthy BALB/c nude mice were intravenously injected with PBS (as control group) and Cu–OCNP/Lap (5 mg/kg), respectively. Mice body weight was recorded every second day, and the blood from mice was then collected for biochemistry analysis after 16 days of injection.

2.20. In vivo biodistribution and excretion of Cu–OCNP/Lap

To evaluate the biodistribution of Cu–OCNP/Lap, the tumor-bearing mice were i.v. injected with Cu–OCNP/Lap, and the major organs and tissues were collected at predetermined time points. The collected organs and tissues were then weighted and dissolved in 2 mL of nitric acid at 70 °C for 12 h. Each sample was diluted with deionized water and corresponding Cu^{2+}/Cu^{+} concentration was determined via ICP-MS. To study the excretion of Cu–OCNP/Lap, Cu–OCNP/Lap injected mice were fed in metabolic cages to collect urine and feces. The collected urine and feces were digested by 2 mL of nitric acid and measured by ICP-MS.

3. Results and discussion

Cu-THQ/AQ4N self-assembled complex was synthesized via metal-organic coordination interaction between Cu^{2+} and C═O/C–O group of AQ4N and THQ, which showed sphere structure with particle size of 47 ± 4.7 nm (Figure S1a), hydrodynamic diameter of 66 ± 3.8 nm (Figure S1b), zeta potential of 15 ± 1.6 mV (Figure S1d) and a broad absorption band covered from visible to NIR-II region (Figure S1e). The successful coordination between Cu^{2+} and AQ4N/THQ showed decrease ratio of C═O characteristic peak at 1604 cm^{-1} over C–N characteristic peat at 1534 cm^{-1} (Fig. 1a) [31]. The amount of Cu^{2+} in Cu-THQ/AQ4N was determined as 142 ng/mg by ICP-MS. N_2 adsorption–desorption isotherm assay indicated 78 m^2/g of surface area and 1.59 nm of pore size for Cu-THQ/AQ4N (Fig. 1b and c), which is appropriate for β-Lap loading. Hydrophobic β-Lap was loaded into Cu-THQ/AQ4N via π–π

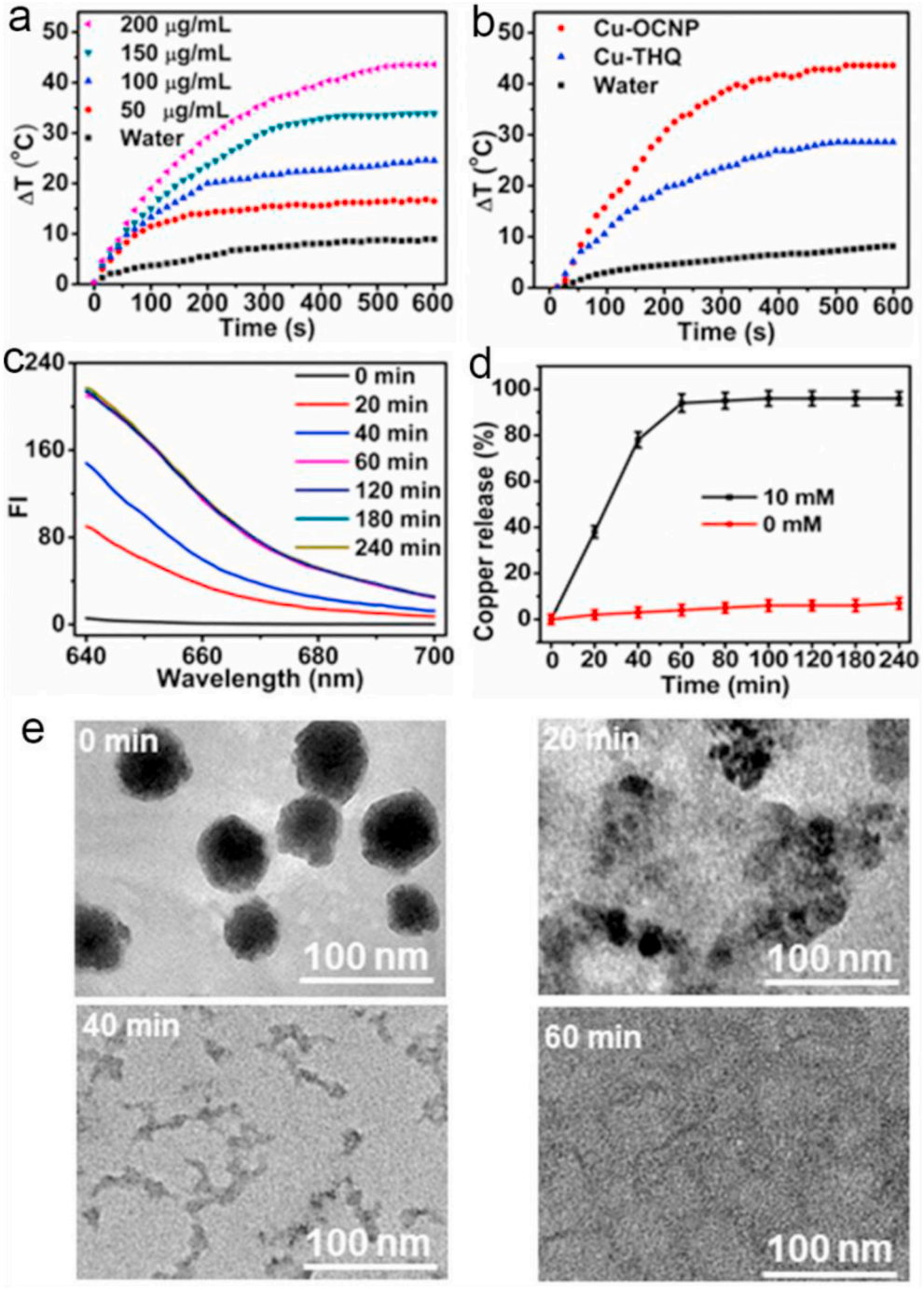

Fig. 2. Temperature change according to 1064 nm laser irradiation time for (a) different concentrations Cu–OCNP and (b) 200 μg/mL Cu–OCNP, Cu-THQ and water c) Fluorescence recovery of AQ4N, d) copper release percentage and e) TEM images of Cu–OCNP according to time via treating Cu–OCNP with GSH. The data error bars in d) indicate means ± SD (n = 4).

stacking and hydrophobic interaction, and PEG-FA with amino terminal group was subsequently conjugated via coordination interaction to get Cu–OCNP/Lap [32]. Cu–OCNP/Lap had particle size of 53 ± 3.1 nm (Fig. 1d) with hydrodynamic diameter of 90 ± 3.6 nm (Figure S1c), and showed characteristic absorption of β-Lap at 258 nm (Fig. 1e). The loading content and loading efficiency of β-Lap in Cu–OCNP/Lap was evaluated as 19.4% and 76.5% by comparing its characteristic absorption intensity with standard calibration curve. The successful conjugation of PEG-FA to Cu-THQ/AQ4N was confirmed by FT-IR spectrum of Cu–OCNP in the absence of β-Lap loading, which showed PEG characteristic absorption peaks at 2935 cm^{-1} and 1097 cm^{-1} corresponding to the stretching vibrations of C–H and C–O–C respectively (Fig. 1a). Cu–OCNP showed zeta potential of −6 ± 1.4 mV (Figure S1d), and increased the intensities of C and O characteristic peaks at 284.8 eV and 531.7 eV in X-ray photoelectron spectroscopy (XPS) spectrum (Figure S1f). Cu–OCNP/Lap showed satisfactory stability upon incubation with cell culture medium DMEM containing 10% fatal bovine serum, as indicated by the stable AQ4N fluorescence (Figure S2a) and unchanged particle size (Figure S2b) upon 24 h incubation.

Due to the photoinduced electrontransfer (PET) mechanism, Cu^{2+} in Cu–OCNP could facilitate nonradiative transition of AQ4N and THQ, thus increases photothermal effect [33]. The fluorescence quenching

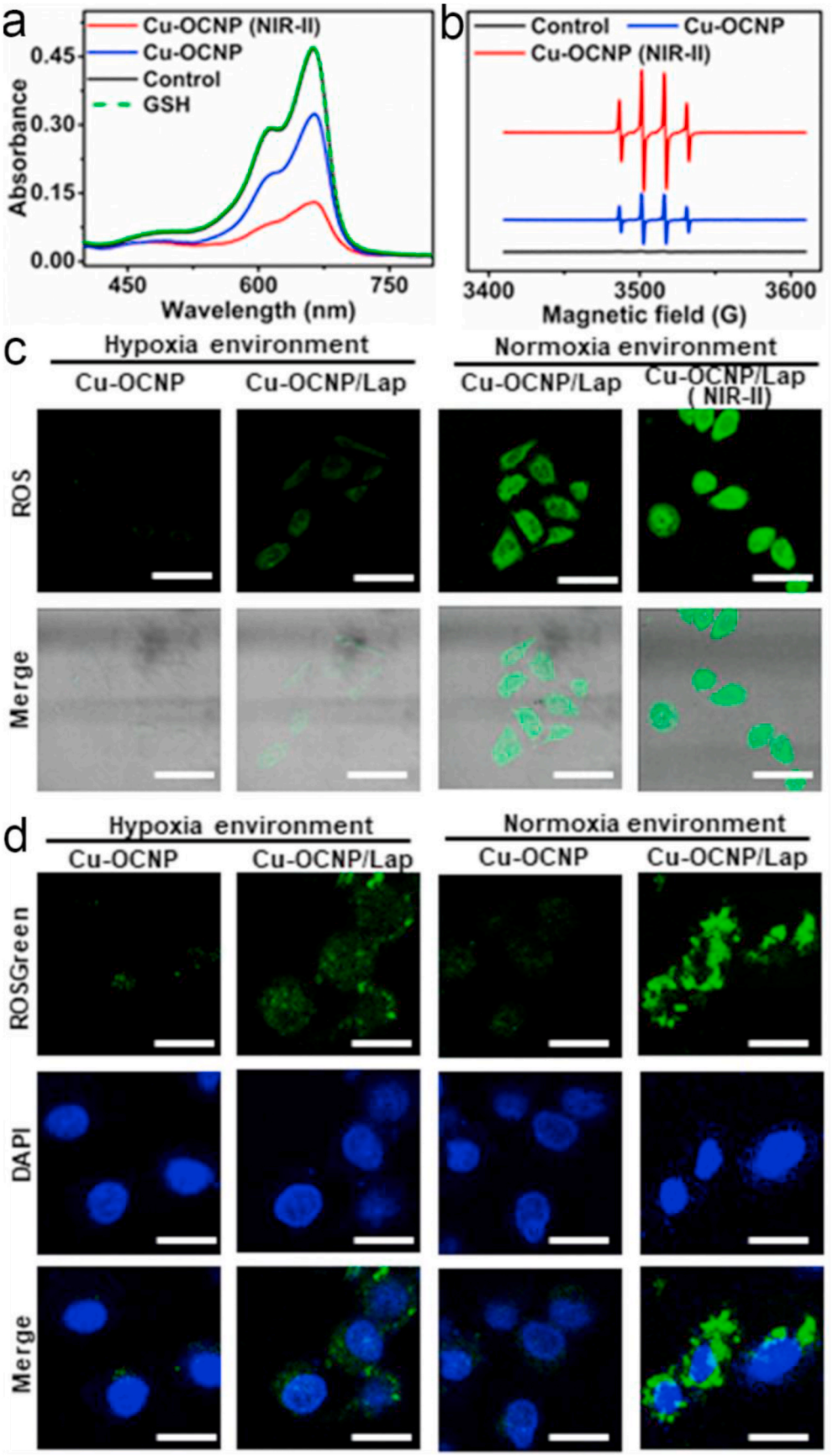

Fig. 3. a) Absorption spectra of MB and b) EPR spectra via incubating Cu–OCNP with GSH and H_2O_2 in the presence and absence of 1064 nm laser irradiation, c) CLSM images of 2′,7′-dichlorofluorescein diacetate (DCFH-DA) stained HeLa cells with different treatment (Scale bar:60 μm), d) CLSM images of H_2O_2 probe ROSGreen stained HeLa cells treated with Cu–OCNP and Cu–OCNP/Lap in hypoxia and normoxia environments (Scale bar: 25 μm).

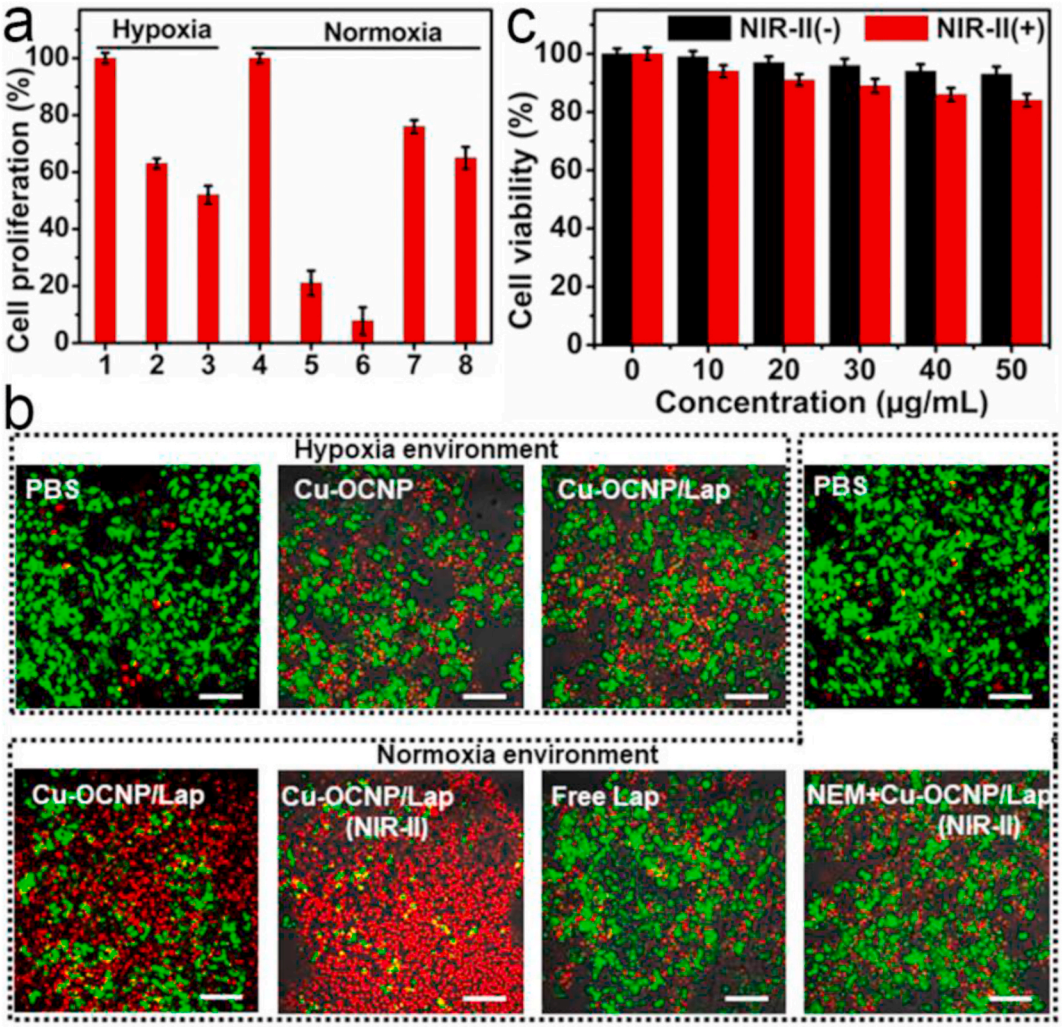

Fig. 4. a) The cell viability percentages of Hela cells treated with 1) PBS, 2) Cu–OCNP, 3) Cu–OCNP/Lap in hypoxia environment, and 4) PBS, 5) Cu–OCNP/Lap, 6) Cu–OCNP/Lap with NIR-II light irradiation, 7) free β-Lap, 8) NEM and Cu–OCNP/Lap with NIR-II light irradiation in normoxia environment, b) CLSM image of calcein-AM/PI stained HeLa cells at different conditions. (Scale bar: 200 μm), c) MTT assay of 3T3 cells treated with different concentrations of Cu–OCNP/Lap in the absence (NIR-II(-)) and presence (NIR-II(+)) of NIR-II light. The data error bars in a) and c) indicate means ± SD (n = 5).

efficiency of AQ4N and THQ were about 97.4% and 98.5%, respectively (Figure S3a, b). The photothermal property of Cu–OCNP was measured by detection solution temperature change, which demonstrated concentration dependent increase and reached 44 °C in 600 s for 200 μg/mL Cu–OCNP (Fig. 2a). In comparison, 200 μg/mL Cu-THQ

coordinated complex only showed 28 °C temperature increase in 600 s (Fig. 2b), indicating the contribution of AQ4N to the photothermal effect of Cu–OCNP. Moreover, Cu–OCNP demonstrated excellent photothermal conversion efficiency of 68.5% (Figure S3c, d). The photoinduced electron transfer from Cu in Cu–OCNP to fluorophore AQ4N and THQ at excited state quenches their fluorescence and increase the photothermal conversion efficiency [31]. The photothermal conversion efficiency is better than some previously reported Cu based photothermal agents (Table S1). In addition, Cu–OCNP showed good thermal stability (Figure S3e).

GSH reduced Cu^{2+} to Cu^{+} and correspondingly diminished its coordination with AQ4N/THQ [34], which resulted sharp fluorescence recovery of AQ4N (Fig. 2c) with 96 ± 1.7% of AQ4N release at 60 min (Figure S4a) and color change of Cu–OCNP solution from light violet to deep purple (Figure S4b). Copper release was monitored by ICP-MS according to time, and reached 97 ± 2.1% at 60 min (Fig. 2d). During the Cu–OCNP degradation process, its morphology continued swelling according to time (Fig. 2e) with polydispersity index (PDI) turned broader (Figure S5). The nanoparticle structure completely disappeared at 60 min, indicating the complete decomposition of Cu/OCNP. Moreover, XPS analysis of GSH treated Cu–OCNP showed that the binding energies of $Cu2p_{1/2}$ and $Cu2p_{3/2}$ slightly shifted from 954.0 to 953.8 eV and 933.9 to 933.5 eV, respectively. The satellite peaks for Cu^{2+} were also disappeared after GSH treatment (Figure S6), confirming the reduction of Cu^{2+} to Cu^{+} by GSH [35]. The GSH responsive degradation of Cu–OCNP and corresponding sufficient release of Cu^{+} guaranteed Fenton-like reaction. In the absence of GSH, Cu–OCNP showed good stability at pH 7.4 (Figure S7a), and slightly degraded at pH 6.5 (Figure S7b) and 5.0 (Figure S7c). The released Cu^{+} catalyzed Fenton-like reaction in the presence of H_2O_2 and produced •OH, which reduced methylene blue (MB) absorbance (Fig. 3a, Cu–OCNP). On the contrary, MB demonstrated stable absorbance in the presence of GSH at pH 6.5 (Fig. 3a, GSH). Electron spin resonance (ESR) spectroscopy was further preformed to confirm •OH generation with 5,5-dimethyl-1-pyrrolineN-oxide (DMPO) as •OH trapping agent, and demonstrated characteristic 1:2:2:1 quartet signal (Fig. 3b, Cu–OCNP). 1064 nm light irradiation further prompted •OH generation, which intensified MB degradation (Fig. 3a, Cu–OCNP (NIR-II)) and enhanced quartet signal intensity in ESR spectroscopy (Fig. 3b, Cu–OCNP (NIR-II)).

Cu–OCNP was then incubated with HeLa cells, and the intracellular AQ4N fluorescence gradually recovered according to time due to the

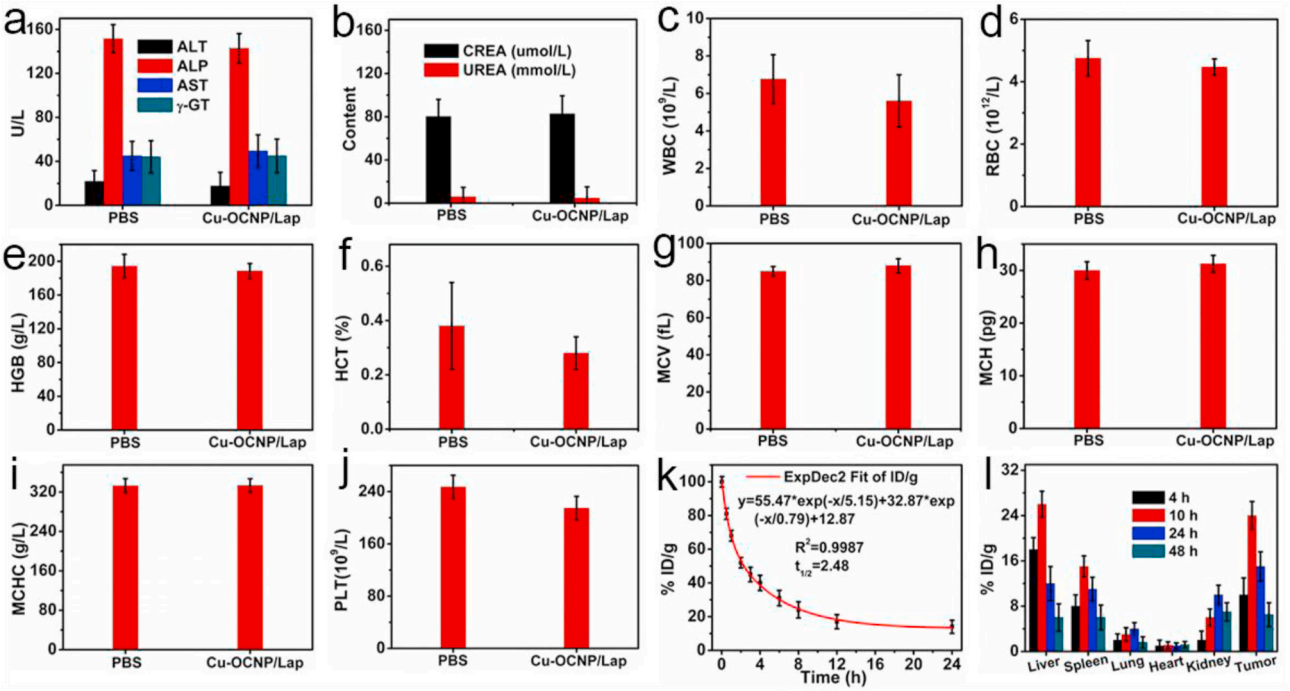

Fig. 5. Biosafety assessment of Cu–OCNP/Lap. a) Hepatic and b) renal functions of mice, Blood analysis results including c) WBC, d) RBC, e) HGB, f) HCT, g) MCV, h) MCH, i) MCHC, j) PLT, k) Pharmacokinetic of Cu–OCNP/Lap after mice i.v. injection, l) Biodistribution of Cu^{2+}/Cu^{+} after injecting Cu–OCNP/Lap for 4, 10, 24, and 48 h. The data error bars in all figures indicate means ± SD (n = 4).

degradation of Cu–OCNP (Figure S8, 4–8 h). On the contrary, GSH-scavenging reagent N-ethylmaleimide (NEM) treated HeLa cells demonstrated weak fluorescence recovery of AQ4N even after 8 h incubation (Figure S8, NEM), indicating the degradation specificity to GSH. Upon the degradation of Cu–OCNP, Cu^{+} was released and reacted with intracellular H_2O_2 to trigger CDT. HeLa cells was incubated in hypoxia condition with 1% O_2 to mimic tumor microenvironment [36], and the generated •OH was measured using ROS probe 2′,7′-dichlorofluorescein diacetate (DCFH-DA). Taking advantage of tumor cell over-expressed (NAD(P)H):(NQO1) enzyme, β-Lap generates a cyclic reaction with its reduced form hydroquinone and conversion O_2 to H_2O_2 [23], which improved •OH generation. Therefore, Cu–OCNP/Lap incubated HeLa cells showed stronger intracellular green fluorescence of DCHF-DA (Fig. 3c, Cu–OCNP/Lap, hypoxia) compared with Cu–OCNP incubated HeLa cells (Fig. 3c, Cu–OCNP, hypoxia). However, the deficient O_2 supply still limited the efficiency of β-Lap cyclic reaction, thus impaired intracellular H_2O_2 generation. Sufficient O_2 supply boosts β-Lap cyclic reaction, and Cu–OCNP/Lap incubated HeLa cells in.

normoxia condition with 21% O_2 demonstrated more intensive intracellular •OH generation with stronger DCFH-DA green fluorescence (Fig. 3c, Cu–OCNP/Lap, normoxia). Photothermal effect of Cu–OCNP further assisted CDT and enhanced •OH generation [37,38], demonstrating the strongest intracellular green fluorescence (Fig. 3c, Cu–OCNP/Lap (NIR II), normoxia). Flow cytometry analysis also showed strongest DCHF-DA fluorescence from Cu–OCNP/Lap incubated HeLa cells in normoxia environment with NIR-II light irradiation (Figure S9a). Efficient intracellular H_2O_2 generation by sufficient O_2 supply was also confirmed by measuring H_2O_2 level. Cu–OCNP/Lap incubated cells showed stronger green fluorescence of H_2O_2 probe ROSGreen compared with Cu–OCNP incubated cells in hypoxia condition (Fig. 3d, hypoxia). In comparision, the enhancement of ROSGreen fluorescence was much stronger for Cu–OCNP/Lap incubated cells in normoxia condition (Fig. 3d, Cu–OCNP/Lap, normoxia), indicating sufficient O_2 supply boosts β-Lap cyclic reaction and intracellular H_2O_2 accumulation.

Flow cytometry analysis also showed similar tendency of stronger ROSGreen fluorescence from Cu–OCNP/Lap incubated cells in normoxia condition (Figure S9b). In accompany with CDT, the tumor antioxidant defense was also alleviated by GSH depletion during Cu–OCNP/Lap degradation process. The intracellular decrease of GSH was quantified with reduced GSH assay kit, which demonstrated GSH levels of 49 ± 2.1% and 35 ± 2.3% for Cu–OCNP/Lap incubated HeLa cells in the absence and present of 1064 nm light irradiation compared with untreated HeLa cells (Figure S10).

MTT assay was used to evaluate the anticancer effect of Cu–OCNP/Lap. Cu–OCNP/Lap incubated HeLa cells demonstrated 52 ± 3.1% of cell viability in hypoxia environment (Fig. 4a, column 3) compared with 64 ± 1.8% for Cu–OCNP incubated HeLa cells (Fig. 4a, column 2) due to the intracellular H_2O_2 supplement from β-Lap cyclic reaction. In comparison, Cu–OCNP/Lap incubated HeLa cells in normoxia environment showed 21 ± 4.2% of cell viability (Fig. 4a, column 5). The sufficient O_2 supply reinforced β-Lap cyclic reaction, and boosted.

CDT effect. Photothermal effect of Cu–OCNP/Lap under 1064 nm light irradiation further suppressed cell viability to 8 ± 4.6% (Fig. 4a, column 6), indicating impressive anticancer capability of Cu–OCNP/Lap. In addition, HeLa cells were pretreated with NEM to suppress intracellular GSH level, which demonstrated about 67% of cell viability when incubated with Cu–OCNP/Lap in the presence of NIR-II light. This indicated the pure PTT effect to cell viability (Fig. 4a, column 8). The live/dead cell assay showed similar results. Cu–OCNP/Lap treated cells in normoxia condition showed higher cell death rate compared with that of in hypoxia condition, and NIR irradiation further enhanced cell death rate (Fig. 4b, Cu–OCNP/Lap, hypoxia; Cu–OCNP/Lap, Cu–OCNP/Lap (NIR-II), normoxia). Though enhancing intracellular H_2O_2 supplement (Figure S11), free β-Lap had limited effect on cell viability (76 ± 2.3%) (Fig. 4a, column 7) with lower cell death rate (Fig. 4b, free Lap, normoxia) only by intracellular H_2O_2 accumulation. Non-cancerous NIH 3T3 cells were incubated with different concentrations of Cu–OCNP/Lap both in the absence and presence of 1064 nm light, which demonstrated above 93% of cell viability in the absence of 1064 nm light and 84% of cell viability in the presence of 1064 nm light (Fig. 4c), respectively. In addition, Cu–OCNP/Lap showed low hemolysis effect, and only 1.9% of

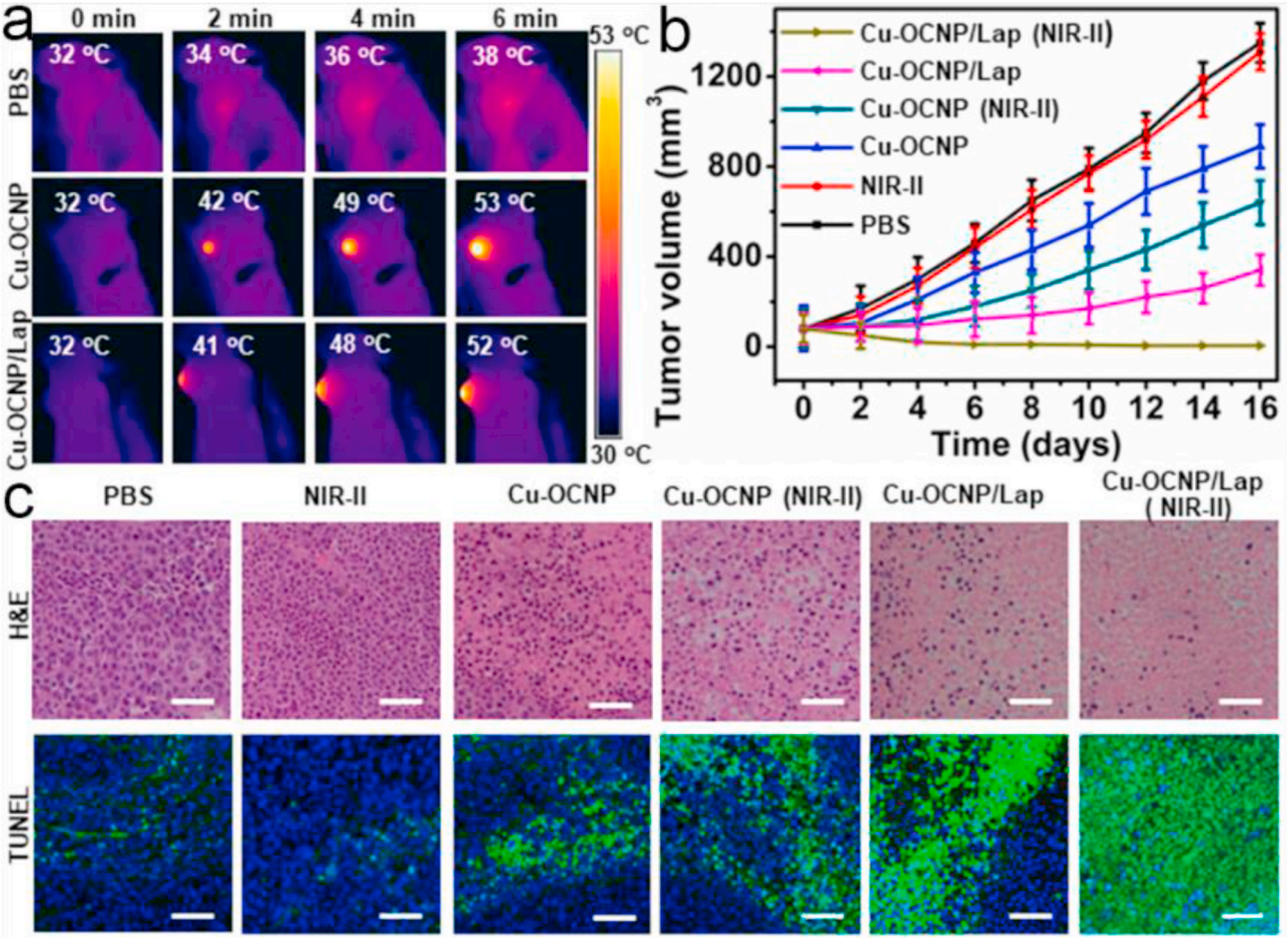

Fig. 6. a) Photothermal images of PBS, Cu–OCNP and Cu–OCNP/Lap injected HeLa tumor-bearing mice with 1064 nm laser irradiation for different times, b) Relative tumor volume at different treatment days and c) histological observations of tumor tissues stained with H&E and TUNEL for HeLa cells tumor-bearing nude mice with different treatment conditions (Scale bar: 100 μm). The data error bars in b) indicate means ± SD (n = 5).

RBCs was hemolyzed even at the concentration of 1000 μg/mL (Figure S12), indicating good biocompatibility of Cu–OCNP/Lap.

To ensure *in vivo* application of Cu–OCNP/Lap, the *in vivo* biosafety of Cu–OCNP/Lap was carried out on healthy BALB/c nude mice by i.v. injection of Cu–OCNP/Lap. As shown in Fig. 5a and b, there were no significant parameter differences between Cu–OCNP/Lap treated mice and PBS treated mice, including ALT, ALP, AST and γ-GT for hepatic function characterization, and CREA and UREA for nephric function characterization. Moreover, after mice were treated with Cu–OCNP/Lap for 16 days, all blood parameters (WBC, RBC, HGB, HCT, MCV, MCH, MCHC and PLT) were in the normal ranges (Fig. 5c–j), indicating good hemocompatibility of Cu–OCNP/Lap. In addition, the pharmacokinetics of Cu–OCNP/Lap was systematically studied by measuring Cu^{2+}/Cu^{+} concentrations in blood at different time points. The blood-circulation half-time of Cu–OCNP/Lap was calculated as 2.48 h following a two-compartment model, which provided a sufficient time period for the effective accumulation of Cu–OCNP/Lap inside the tumor (Fig. 5k). Furthermore, the biodistribution of Cu–OCNP/Lap was studied by measuring Cu^{2+}/Cu^{+} content at tumor sites and main organs by ICP-MS. Cu–OCNP/Lap showed maximum accumulation in tumor site at 10 h post injection. It also accumulated in liver and spleen (Fig. 5l). The accumulation of Cu–OCNP/Lap in organs and tumor tissues were decreased at 24 h and 48 h post administration due to the degradation of nanoparticle. Time-dependent *in vivo* fluorescence imaging and PA imaging of mice showed similar accumulation trend of Cy5-labelled Cu–OCNP/Lap with strongest fluorescence and PA intensity at 10 h post i.v. injection (Figure S13). Cu–OCNP/Lap was degraded by GSH and mainly excreted by bile into feces and kidney into urine, its long-term toxicity was investigated by measuring Cu^{2+}/Cu^{+} content in feces and urine at different time points after administration. The discharge amount was gradually reduced according to time and the discharge percentage reached about 82% at day 6, indicating good biosafety of Cu–OCNP/Lap (Figure S14).

The *in vivo* therapeutic effect of Cu–OCNP/Lap was evaluated with tumor-bearing nude mice. The tumor grown positions were irradiated with 1064 nm laser for different times at 10 h post intravenous injection of Cu–OCNP/Lap and Cu–OCNP respectively, and the tumor temperature reached 52 °C and 53 °C with 6 min irradiation, while the temperature for PBS injected mice was only 38 °C (Fig. 6a, Figure S15). The effective local temperature increase accelerates blood flow, which prompts the level of O_2 content in tumor site to overcome the tumor hypoxia condition [39–41]. Photoacoustic (PA) imaging showed prominent increase of hemoglobin hemoglobin oxygen saturation (sO_2) in tumor site from 11 ± 2.4% for PBS treated and 10 ± 2.3% for Cu–OCNP/Lap treated mice to 92 ± 3.1% for Cu–OCNP/Lap treated mice with NIR-II irradiation (Figure S16), indicating the effective alleviation of tumor hypoxia condition. Tumor slices also demonstrated the down-regulation of hypoxia-inducible factor (HIF)-1α (Figure S17) and abundant H_2O_2 accumulation (Figure S18) for Cu–OCNP/Lap treated mice after 1064 nm light irradiation. The abundant intracellular H_2O_2 supply reinforced β-Lap cyclic reaction and boosted CDT, which demonstrated prominent inhibition to tumor growth for the mice group treated with Cu–OCNP/Lap under 1064 nm light irradiation (Fig. 6b, Figure S19a, b). H&E images also demonstrated maximum necrosis of

tumor cells, and TUNEL images showed highest level of cell apoptosis for Cu–OCNP/Lap treated mice under 1064 nm light irradiation (Fig. 6c). However, only NIR-II irradiation group barely showed inhibition to tumor growth (Fig. 6b, c, Figure S19a, b). The mice body weight remained at similar level for different mice groups during the treatment process (Figure S19c), and no obvious pathological abnormalities was observed in normal organs (Figure S20). These results indicated satisfactory biocompatibility and therapeutic specificity of Cu–OCNP/Lap.

4. Conclusions

In conclusion, we have developed a self-assembled metal-organic coordinated nanoparticle with the loading of intracellular cyclic reaction trigger β-Lap (Cu–OCNP/Lap) for enhanced CDT with abundant H_2O_2 supply. It demonstrated good photothermal property under NIR II light irradiation, which elevated oxygen level in tumor site by accelerating blood flow. In response to intracellular GSH, Cu–OCNP/Lap was decomposed with the release of Cu^+ and β-Lap. Elevated oxygen supply in tumor sites reinforced β-Lap cyclic reaction and provided abundant intracellular H_2O_2 to enhance CDT. In the meanwhile, GSH expression was also eliminated for the alleviation of tumor antioxidant defence to further enhance CDT. Both cellular and *in vivo* results demonstrated good therapeutic effects. We believe that the designed strategy would provide new insight for improving CDT efficiency and benefit tumor therapy.

Data availability statement

The authors declare no competing financial interest.

Declaration of competing interest

The authors declare that they have no known competing financial interests or personal relationships that could have appeared to influence the work reported in this paper.

Acknowledgements

We gratefully acknowledge the National Natural Science Foundation of China (21974064, 22022405, 21635005), Natural Science Foundation of Jiangsu Province for distinguished Young Scholars (BK20200010), Specially-appointed Professor Foundation of Jiangsu Province, Program for Innovative Talents and Entrepreneurs of Jiangsu Province, National Natural Science Foundation of China (21805118).

Appendix A. Supplementary data

Supplementary data to this article can be found online at https://doi.org/10.1016/j.biomaterials.2021.120962.

Credit author statement

Yuling He: Designing strategies, Performing experiments, Analyzing data, Writing manuscript, Shuwen Guo: Analyzing data, Yue Zhang: Performing experiments, Ying Liu: Supervision, Designing strategies, Writing manuscript, Huangxian Ju: Supervision.

References

[1] D. Wang, H. Wu, G. Yang, C. Qian, L. Gu, H. Wang, W. Zhou, J. Liu, Y. Wu, X. Zhang, Z. Guo, H. Chen, D. Jana, Y. Zhao, Metal-organic framework derived multicomponent nanoagent as a reactive oxygen species amplifier for enhanced photodynamic therapy, ACS Nano 14 (2020) 13500–13511.

[2] J. Lin, T. He, Y. Yuan, C. Jiang, N.T. Blum, J. He, P. Huang, Light-triggered transformable ferrous ion delivery system for photothermal primed chemodynamic therapy, Angew. Chem. Int. Ed. (2020), https://doi.org/10.1002/anie.202015379.

[3] S. Fu, R. Yang, L. Zhang, W. Liu, G. Du, Y. Cao, Z. Xu, H. Cui, Y. Kang, P. Xue, Biomimetic CoO@AuPt nanozyme responsive to multiple tumor microenvironmental clues for augmenting chemodynamic therapy, Biomaterials 257 (2020) 120279.

[4] Z. Tang, Y. Liu, M. He, W. Bu, Chemodynamic therapy: tumour microenvironment-mediated Fenton and fenton-like reactions, Angew. Chem. Int. Ed. 58 (2019) 946–956.

[5] B. Yang, Y. Chen, J. Shi, Reactive oxygen species (ROS)-Based nanomedicine, Chem. Rev. 119 (2019) 4881–4985.

[6] H. Lin, Y. Chen, J. Shi, Nanoparticle-triggered in situ catalytic chemical reactions for tumour-specific therapy, Chem. Soc. Rev. 47 (2018) 1938–1958.

[7] Y. Sang, F. Cao, W. Li, L. Zhang, Y. You, Q. Deng, K. Dong, J. Ren, X. Qu, Bioinspired construction of a nanozyme-based H_2O_2 homeostasis disruptor for intensive chemodynamic therapy, J. Am. Chem. Soc. 142 (2020) 5177–5183.

[8] J. Shen, T.W. Rees, Z. Zhou, S. Yang, L. Ji, H. Chao, A mitochondria-targeting magnetothermogenic nanozyme for magnet-induced synergistic cancer therapy, Biomaterials 251 (2020) 120079.

[9] B. Yang, J. Shi, Ascorbate tumor chemotherapy by an iron-engineered nanomedicine-catalyzed tumor-specific pro-oxidation, J. Am. Chem. Soc. 142 (2020) 21775–21785.

[10] J. Liu, Q. Chen, L. Feng, Z. Liu, Nanomedicine for tumor microenvironment modulation and cancer treatment enhancement, Nano Today 21 (2018) 55–73.

[11] M. Wang, M. Chang, Q. Chen, D. Wang, C. Li, Z. Hou, J. Lin, D. Jin, B. Xing, Au_2Pt-PEG-Ce6 nanoformulation with dual nanozyme activities for synergistic chemodynamic therapy/phototherapy, Biomaterials 252 (2020) 120093.

[12] C. Fang, Z. Deng, G. Cao, Q. Chu, Y. Wu, X. Li, X. Peng, G. Han, Co–Ferrocene MOF/glucose oxidase as cascade nanozyme for effective tumor therapy, Adv. Funct. Mater. 30 (2020) 1910085.

[13] Y. Zhao, D. Wang, H. Wu, C. Wang, L. Gu, H. Chen, D. Jana, X. Wang, P. Xu, Z. Guo, Q. Chen, L. Feng, J. Liu, Self-assembled single-site nanozyme for tumor-specific amplified cascade enzymatic therapy, Angew. Chem. Int. Ed. (2020), https://doi.org/10.1002/anie.202008868.

[14] Y. Liu, W. Zhen, Y. Wang, S. Song, H. Zhang, $Na_2S_2O_8$ nanoparticles trigger antitumor immunotherapy through reactive oxygen species storm and surge of tumor osmolarity, J. Am. Chem. Soc. 142 (2020) 21751–21757.

[15] Y. Wang, L. Shi, Z. Ye, K. Guan, L. Teng, J. Wu, X. Yin, G. Song, X.B. Zhang, Reactive oxygen correlated chemiluminescent imaging of a semiconducting polymer nanoplatform for monitoring chemodynamic therapy, Nano Lett. 20 (2020) 176–183.

[16] S. Sanchez-Casanova, F.M. Martin-Saavedra, C. Escudero-Duch, M.I. Falguera Uceda, M. Prieto, M. Arruebo, P. Acebo, M.L. Fabiilli, R.T. Franceschi, N. Vilaboa, Local delivery of bone morphogenetic protein-2 from near infrared-responsive hydrogels for bone tissue regeneration, Biomaterials 241 (2020) 119909.

[17] X. Liu, Z. Liu, K. Dong, S. Wu, Y. Sang, T. Cui, Y. Zhou, J. Ren, X. Qu, Tumor-activatable ultrasmall nanozyme generator for enhanced penetration and deep catalytic therapy, Biomaterials 258 (2020) 120263.

[18] X. Wan, L. Song, W. Pan, H. Zhong, N. Li, B. Tang, Tumor-targeted cascade nanoreactor based on metal-organic frameworks for synergistic ferroptosis-starvation anticancer therapy, ACS Nano 14 (2020) 11017–11028.

[19] G. Gadda Fan, On the catalytic mechanism of choline oxidase, J. Am. Chem. Soc. 127 (2005) 2067–2074.

[20] Z. Ren, S. Sun, R. Sun, G. Cui, L. Hong, B. Rao, A. Li, Z. Yu, Q. Kan, Z. Mao, A metal-polyphenol-coordinated nanomedicine for synergistic cascade cancer chemotherapy and chemodynamic therapy, Adv. Mater. 32 (2020) 1906024.

[21] L. Lin, S. Wang, H. Deng, W. Yang, L. Rao, R. Tian, Y. Liu, G. Yu, Z. Zhou, J. Song, H.-H. Yang, Z.-Y. Chen, X. Chen, Endogenous labile iron pool-mediated free radical generation for cancer chemodynamic therapy, J. Am. Chem. Soc. 142 (2020) 15320–15330.

[22] L.S. Lin, T. Huang, J. Song, X.Y. Ou, Z. Wang, H. Deng, R. Tian, Y. Liu, J.F. Wang, Y. Liu, G. Yu, Z. Zhou, S. Wang, G. Niu, H.H. Yang, X. Chen, Synthesis of copper peroxide nanodots for H_2O_2 self-supplying chemodynamic therapy, J. Am. Chem. Soc. 141 (2019) 9937–9945.

[23] Y. Wu, X. Wang, S. Chang, W. Lu, M. Liu, X. Pang, Beta-lapachone induces NAD(P)H:quinone oxidoreductase-1- and oxidative stress-dependent heat shock protein 90 cleavage and inhibits tumor growth and angiogenesis, J. Pharmacol. Exp. Therapeut. 357 (2016) 466–475.

[24] L. Torrente, N. Prieto-Farigua, A. Falzone, C.M. Elkins, D.A. Boothman, E.B. Haura, G.M. DeNicola, Inhibition of TXNRD or SOD1 overcomes NRF_2-mediated resistance to beta-lapachone, Redox biology 30 (2020) 101440.

[25] J.J. Hu, M.D. Liu, F. Gao, Y. Chen, S.Y. Peng, Z.H. Li, H. Cheng, X.Z. Zhang, Photo-controlled liquid metal nanoparticle-enzyme for starvation/photothermal therapy of tumor by win-win cooperation, Biomaterials 217 (2019) 119303.

[26] J. Xu, R. Shi, G. Chen, S. Dong, P. Yang, Z. Zhang, N. Niu, S. Gai, F. He, Y. Fu, J. Lin, All-in-One theranostic nanomedicine with ultrabright second near-infrared emission for tumor-modulated bioimaging and chemodynamic/photodynamic therapy, ACS Nano 14 (2020) 9613–9625.

[27] G. Chen, Y. Yang, Q. Xu, M. Ling, H. Lin, W. Ma, R. Sun, Y. Xu, X. Liu, N. Li, Z. Yu, M. Yu, Self-amplification of tumor oxidative stress with degradable metallic complexes for synergistic cascade tumor therapy, Nano Lett. 20 (2020) 8141–8150.

[28] Z. Zhou, H. Wu, R. Yang, A. Xu, Q. Zhang, J. Dong, C. Qian, M. Sun, GSH depletion liposome adjuvant for augmenting the photothermal immunotherapy of breast cancer, Sci. Adv. 6 (2020) 4373.

[29] Y. Wang, W. Du, T. Zhang, Y. Zhu, Y. Ni, C. Wang, F.M. Sierra Raya, L. Zou, L. Wang, G. Liang, A self-evaluating photothermal therapeutic nanoparticle, ACS Nano 14 (2020) 9585–9593.

[30] Y. Yang, X. Fan, L. Li, Y. Yang, A. Nuernisha, D. Xue, C. He, J. Qian, Q. Hu, H. Chen, J. Liu, W. Huang, Semiconducting polymer nanoparticles as theranostic system for

near-infrared-II fluorescence imaging and photothermal therapy under safe laser fluence, ACS Nano 14 (2020) 2509–2521.
[31] D. Zhang, H. Xu, X. Zhang, Y. Liu, M. Wu, J. Li, H. Yang, G. Liu, X. Liu, J. Liu, Z. Yuan, Self-quenched metal-organic particles as dual-mode therapeutic agents for photoacoustic imaging-guided second near-infrared window photochemotherapy, ACS Appl. Mater. Interfaces 10 (2018) 25203–25212.
[32] E.I. Solomon, D.E. Heppner, E.M. Johnston, J.W. Ginsbach, J. Cirera, M. Qayyum, M.T. Kieber-Emmons, C.H. Kjaergaard, R.G. Hadt, L. Tian, Copper active sites in biology, Chem. Rev. 114 (2014) 3659–3853.
[33] A.M.D.C. Ferreira, M.R. Ciriolo, L. Marcocci, G. Rotilio, Copper(I) transfer into metallothionein mediated by glutathione, Biochem. J. 292 (1993) 673–676.
[34] G. Liu, J. Zhu, H. Guo, A. Sun, P. Chen, L. Xi, W. Huang, X. Song, X. Dong, Mo_2C-Derived polyoxometalate for NIR-II photoacoustic imaging-guided chemodynamic/photothermal synergistic therapy, Angew. Chem. Int. Ed. 58 (2019) 18641–18646.
[35] B. Ma, S. Wang, F. Liu, S. Zhang, J. Duan, Z. Li, Y. Kong, Y. Sang, H. Liu, W. Bu, L. Li, Self-assembled copper-amino acid nanoparticles for in situ glutathione "AND" H_2O_2 sequentially triggered chemodynamic therapy, J. Am. Chem. Soc. 141 (2019) 849–857.
[36] A. Carreau, B. El Hafny-Rahbi, A. Matejuk, C. Grillon, C. Kieda, Why is the partial oxygen pressure of human tissues a crucial parameter Small molecules and hypoxia, J. Cell Mol. Med. 15 (2011) 1239–1253.
[37] S. Sun, Q. Chen, Z. Tang, C. Liu, Z. Li, A. Wu, H. Lin, Tumor microenvironment stimuli-responsive fluorescence imaging and synergistic cancer therapy by carbon-dot–Cu^{2+} nanoassemblies, Angew. Chem. Int. Ed. 59 (2020) 21041–21048.
[38] F. Jiang, B. Ding, S. Liang, Y. Zhao, Z. Cheng, B. Xing, P.a. Ma, J. Lin, Intelligent MoS_2–CuO heterostructures with multiplexed imaging and remarkably enhanced antitumor efficacy via synergetic photothermal therapy/chemodynamic therapy/immunotherapy, Biomaterials 268 (2021) 120545.
[39] J. Chen, M. Li, X. Yi, Q. Zhao, L. Chen, C. Yang, J. Wu, K. Yang, Synergistic effect of thermo-radiotherapy using Au@FeS core-shell nanoparticles as multifunctional therapeutic nanoagents, Part. Part. Syst. Char. 34 (2017) 1600330.
[40] Y. Liu, Y. Jiang, M. Zhang, Z. Tang, M. He, W. Bu, Modulating hypoxia via nanomaterials Chemistry for efficient treatment of solid tumors, Acc. Chem. Res. 51 (2018) 2502–2511.
[41] C.S. Jin, J.F. Lovell, J. Chen, G. Zheng, Ablation of hypoxic tumors with dose-equivalent photothermal, but not photodynamic, therapy using a nanostructured porphyrin assembly, ACS Nano 7 (2013) 2541–2550.